JOURNAL OF GEOPHYSICAL RESEARCH: SOLID EARTH, VOL. 118, 2965–2981, doi:10.1002/jgrb.50216, 2013

Intense interface seismicity triggered by a shallow slow slip event in the Central Ecuador subduction zone

Martin Vallée,[1,2] Jean-Mathieu Nocquet,[1] Jean Battaglia,[3] Yvonne Font,[1] Monica Segovia,[4] Marc Régnier,[1] Patricia Mothes,[4] Paul Jarrin,[4] David Cisneros,[5] Sandro Vaca,[4] Hugo Yepes,[4] Xavier Martin,[1] Nicole Béthoux,[1] and Mohamed Chlieh[1]

Received 13 November 2012; revised 7 May 2013; accepted 8 May 2013; published 17 June 2013.

[1] We document a 1 week long slow slip event (SSE) with an equivalent moment magnitude of 6.0–6.3 which occurred in August 2010 below La Plata Island (Ecuador), south of the rupture area of the 1906 Mw = 8.8 megathrust earthquake. GPS data reveal that the SSE occurred at a depth of about 10 km, within the downdip part of a shallow (<15 km), isolated, locked patch along the subduction interface. The availability of both broadband seismometer and continuous geodetic station located at the La Plata Island, 10 km above the SSE, enables a careful analysis of the relationships between slow and rapid processes of stress release along the subduction interface. During the slow slip sequence, the seismic data show a sharp increase of the local seismicity, with more than 650 earthquakes detected, among which 50 have a moment magnitude between 1.8 and 4.1. However, the cumulative moment released through earthquakes accounts, at most, for 0.2% of the total moment release estimated from GPS displacements. Most of the largest earthquakes are located along or very close to the subduction interface with focal mechanism consistent with the relative plate motion. While the earthquake sizes show a classical distribution (Gutenberg-Richter law with a b-value close to 1), the space-time occurrence presents a specific pattern. First, the largest earthquakes appear to occur randomly during the slow slip sequence, which further evidence that the seismicity is driven by the stress fluctuations related to aseismic slip. Moreover, the seismicity observed during the SSE consists in individual events and families of repeating earthquakes. These observations indicate that the stress increment induced by the episodic aseismic slip may lead both to sudden seismic moment release and to progressive rupture within small locked patches. This study offers an a posteriori interpretation of the seismogenesis in the Central Ecuador subduction zone, where intense seismic swarms have been regularly observed (1977, 1998, 2002, and 2005). These swarms have likely been triggered by large-magnitude slow slip events.

Citation: Vallée, M., et al. (2013), Intense interface seismicity triggered by a shallow slow slip event in the Central Ecuador subduction zone, *J. Geophys. Res. Solid Earth*, *118*, 2965–2981, doi:10.1002/jgrb.50216.

1. Introduction

[2] Slow slip events (SSEs) have been documented in numerous segments of the circum-Pacific subduction zone (Cascades, Japan, Mexico, and Costa Rica; see *Schwartz and Rokosky* [2007] for a review). These SSEs, which can last from days to months, occur along the subduction interface with a mechanism releasing some of the stress accumulated by plate convergence. First observed at depths of 30–50 km, close to the downdip limit of strongly coupled subduction interfaces (southwest Japan [*Hirose et al*., 1999] and Cascades [*Dragert et al*., 2001]), they were interpreted as the expression of the brittle-ductile transition zone located at the downdip limit of the seismogenic zone. Above this zone and up to shallow depths, the interface accumulates slip deficit, which is mostly released during large megathrust earthquakes. Below it, the plates are freely slipping. More recently, SSEs were also observed at shallower depths, at least in three subduction zones (Boso Peninsula, Japan [*Ozawa et al*., 2003; *Sagiya*, 2004]; Hikurangi, New Zealand [*Douglas et al*., 2005; *McCaffrey et al*., 2008; *Wallace and Beavan*, 2010]; and Nicoya, Costa Rica [*Outerbridge et al*., 2010]). Nonetheless, in the two latter cases (Hikurangi, northern New Zealand, and Costa Rica), the locus of the SSEs is consistent with the view of a downdip

Additional supporting information may be found in the online version of this article.

[1]Geoazur, Université de Nice Sophia-Antipolis, IRD-CNRS-OCA, Nice, France.
[2]Now at Institut de Physique du Globe de Paris, Sorbonne Paris Cité, Université Paris Diderot, UMR 7154 CNRS, Paris, France.
[3]Laboratoire Magmas et Volcans, Université Blaise Pascal-CNRS-IRD, Clermont-Ferrand, France.
[4]Instituto Geofísico, Escuela Politécnica Nacional, Quito, Ecuador.
[5]IGM-EC, Military Geographic Institute of Ecuador, Quito, Ecuador.

Corresponding author: M. Vallée, Institut de Physique du Globe de Paris, Sorbonne Paris Cité, Université Paris Diderot, UMR 7154 CNRS, 75005 Paris, France. (vallee@ipgp.fr)

2169-9313/13/10.1002/jgrb.50216

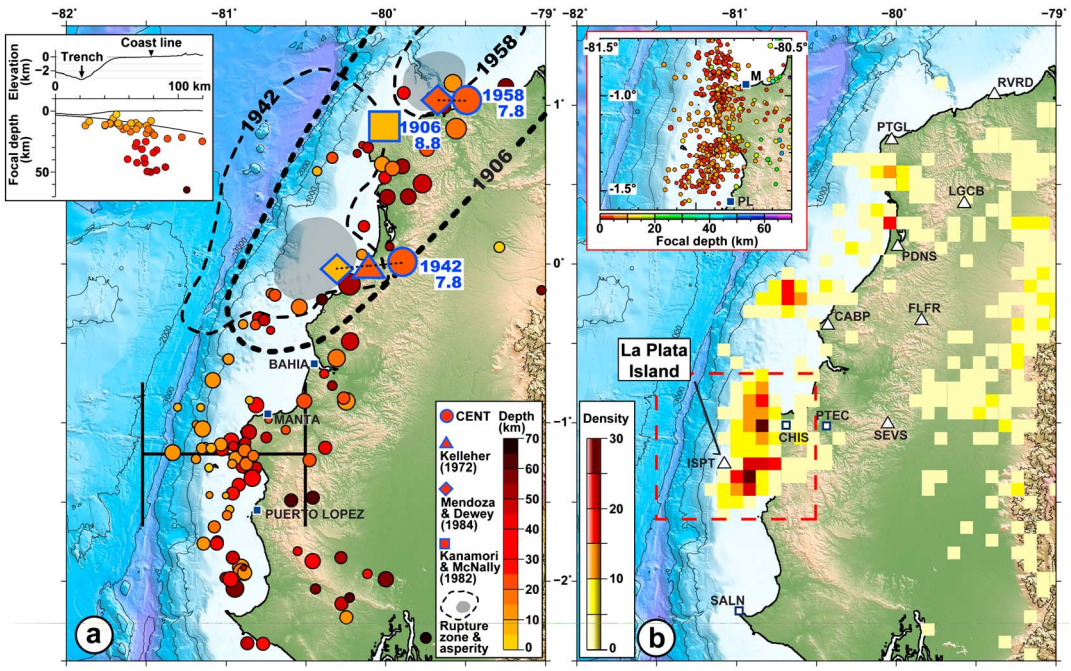

Figure 1. Seismicity of the Ecuadorian subduction zone. (a) Map of earthquake epicenters and rupture area of major earthquakes. Black-contoured circles are earthquakes from the EHB catalog [*Engdahl et al*., 1998] for the 1960–2007 period. Depth is indicated by the color scale, and the symbol size is relative to Mb magnitudes, ranging from 3.8 to 6.5. The epicenters of historical earthquakes compiled from several studies are blue contoured (CENT stands for the Centennial catalog of *Engdahl and Villaseñor* [2002]). Rupture zones and asperity locations are from *Beck and Ruff* [1984] and *Swenson and Beck* [1996]. The inset shows the east-west cross section (location and width are marked on the map), with black lines representing topography and top of the subducting Nazca Plate (modified after *Graindorge et al*. [2004]). (b) Earthquake density map from a relocation work [*Font et al*., 2013] of the local network catalog (1994–2007; IG-EPN). Cells including only one earthquake are not shown. Relocated earthquakes within the red dashed box are shown in the upper left inset. The continuous stations (seismometer and GPS) of the ADN project (installed in 2008–2009) are shown by triangles. Two permanent GPS stations of the IG-EPN (CHIS and SALN) and one (PTEC) from the Military Geographic Institute (IGM) are shown by squares. In both figures, bathymetry is contoured and labeled (in m).

brittle-ductile transition zone, as the locking depth is shallow in these two areas. The case of the Boso Peninsula shows a more complex pattern, because the location of the 1996 SSE appears to be adjacent to a coupled zone [*Sagiya*, 2004].

[3] Since the discovery of SSEs, this proximity between the slow slip processes and earthquake-prone areas has raised the question of their seismic triggering potential [e.g., *Dragert et al*., 2001; *Mazzotti and Adams*, 2004]. As a matter of fact, although SSEs should inhibit the seismic rupture where they occur, the stress increment they induce may promote the seismic rupture in the surrounding fault segments when near to failure. The close relationships between SSEs and seismic processes have been evidenced but usually not with classical seismicity: SSEs are often shown to be accompanied by a peculiar seismic activity, referred to as nonvolcanic tremors (NVTs) [*Rogers and Dragert*, 2003]. These NVTs clearly differ from the usual seismicity because of their long duration and absence of clear wave arrivals. So far, triggering of large interplate earthquakes by slow slip events has not been observed, although aseismic slip has been proposed to precede the 2011 Tohoku (Japan) earthquake [*Kato et al*., 2012]. Concerning the lower magnitude seismicity, earthquakes rate has been shown to clearly increase during the SSEs in only two subduction areas, namely, the Boso Peninsula [*Ozawa et al*., 2003; *Sagiya*, 2004] and the Hikurangi subduction zone [*Delahaye et al*., 2009]. In the case of the Guerrero SSEs (Mexico), *Liu et al*. [2007] have identified some changes of the seismicity pattern, but they were clearer at the beginning and end of the SSEs than during the process itself. An observation shared by these SSEs is that direct seismic triggering appears to be mainly restricted to shallow SSEs [*Delahaye et al*., 2009], even if a recent study [*Vidale et al*., 2011] also points out the triggering of a few earthquakes during a 2010 SSE in the Cascades region. In the case of the Hikurangi subduction zone, *Delahaye et al*. [2009] have shown some properties of this associated seismicity. In particular, they show that seismicity is consistent with reverse faulting downdip of the SSE, on or close to the subduction interface.

[4] In this study, we first introduce some characteristics of the Central Ecuador subduction zone (see Figure 1) in terms of seismicity and coupling derived from GPS and show that Central Ecuador shares some common characteristics with the northern Hikurangi (New Zealand) subduction zone. More specifically, the interseismic coupling is restricted to the shallower part of the interface located between the trench and La Plata Island. In this context, a shallow SSE occurred during 1 week, in August 2010, within the lower part of the

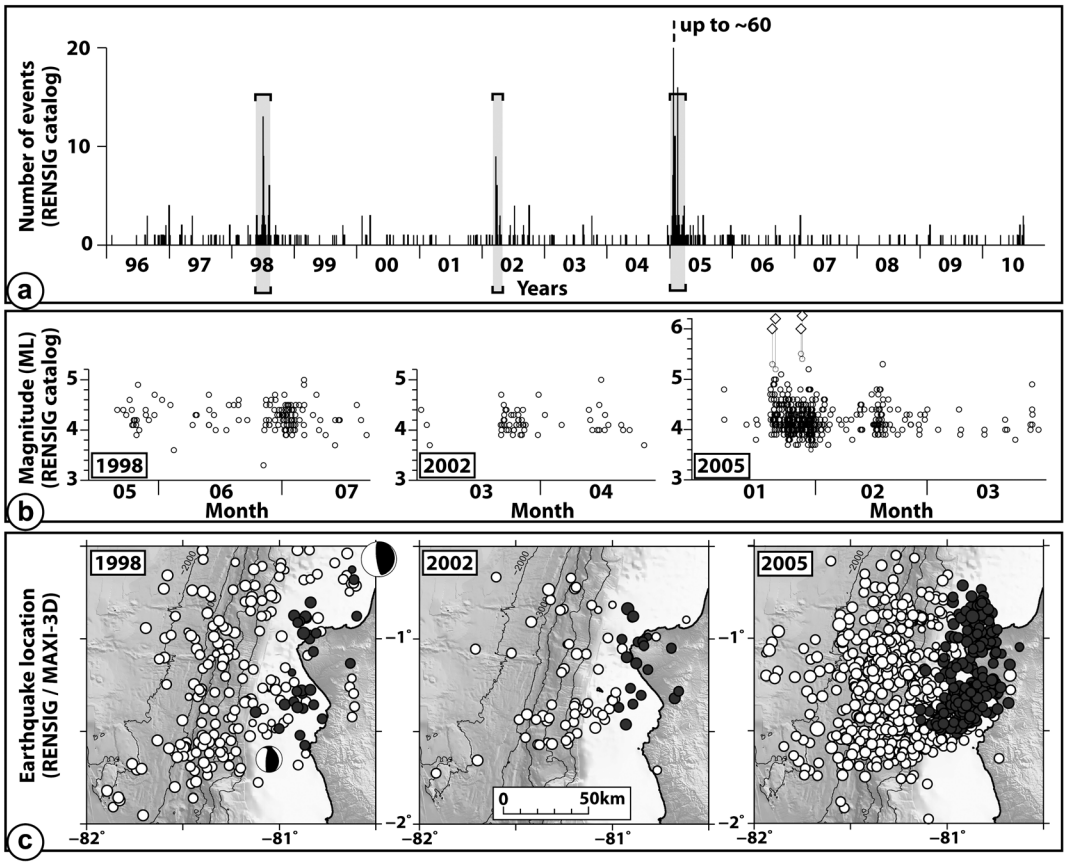

Figure 2. Earthquake occurrence characteristics in the La Plata-Manta region (corresponding to the dashed red box in Figure 1b). (a) Histogram of earthquake occurrence (RENSIG catalog) from 1996 to 2010 (bin is 1 day). (b) Earthquake magnitude versus time for the three main periods of activity. ML is represented by circles (from RENSIG) and Mw by diamonds [*Vaca et al*., 2009]. (c) Epicentral locations (RENSIG) of earthquakes presented in Figure 2b are shown by white circles. Relocations in a 3-D model (MAXI-3D catalog) [*Theunissen et al*., 2012; *Font et al*., 2013] are shown by grey circles. Focal mechanisms of earthquakes with magnitude above ~5.5 are from Global CMT [*Ekström et al*., 2012].

coupled interface. The geometry of observation is unusual and favorable, as we benefit from a GPS and seismic station located on the La Plata Island (Figure 1), only 35 km from the trench and, as will be shown, directly above the 10 km deep slow slip area. Seismic data reveal a strong and abrupt change of the microseismicity during the SSE. We describe how this seismicity is organized—in terms of location, time, and mechanisms—and how it is intimately related to the slow slip itself. This study confirms and further documents the seismic triggering potential of SSEs, even if it is restricted in this particular case to small earthquakes. Moreover, the swarm nature of the seismic crisis, together with the frequent past occurrence of large swarms in this area, indicates that slow slip processes play an important role in the stress release along this segment of the Nazca/South America subduction zone.

2. Seismicity and Interseismic Coupling Along the Central Ecuador Subduction Zone

[5] The Central Ecuador margin is a peculiar region of the North Andean subduction zone. While megathrust earthquakes (moment magnitude larger than 7.7) have been observed north of the latitude ~0.5°S in 1906, 1942, 1958, and 1979 (Figure 1) [*Kelleher,* 1972; *Kanamori and McNally*, 1982; *Mendoza and Dewey*, 1984], they seem to be absent in southern Ecuador and northern Peru [*Dorbath et al*., 1990; *Bilek*, 2010]. Seismically, the region located at latitude ~1°S (offshore Bahia and Manta) thus appears to be a transitional area, delimiting the termination of the major earthquakes activity. However, this simple observation is reversed if looking at the moderate to strong (up to magnitude of 6.5) earthquakes, detected by the global networks since 1960 (Figure 1a) [*Manchuel et al*., 2011]: For this range of magnitudes, the seismic activity is higher around 1°S than in northern Ecuador.

[6] This observation is further confirmed by the characteristics of the local seismicity. We make use of the 1994–2007 local catalog (RENSIG, Red Nacional de Sismógrafos) provided by the Institute of Geophysics of Quito (IG-EPN). Earthquakes of this catalog have been relocated using the MAXI technique [*Font et al*., 2004; *Theunissen et al*., 2012], an a priori 3-D velocity model, and a selection of seismic stations [*Font et al*., 2013], resulting in the *MAXI-3D* catalog. The a priori 3-D velocity model is constructed from the integration of independent geophysical and geological data (see *Font et al*. [2013] for references). The regional model represents the upper crust and mantle intricacies of the subduction zone and associated velocity gradients such as the surface

topography variations (from the oceanic trench to the volcanic arc), the compositional difference between the oceanic subducting plate and the oceanic/continental overriding plate, the lateral seismic velocity variations produced by local tectonic structures (such as the subducting Carnegie Ridge, the fore-arc sedimentary basins, or the back-arc basins), the crustal thickness, and Moho discontinuity. Close to La Plata Island (Figure 1), the knowledge of crustal structure benefits from marine geophysical surveys [*Graindorge et al.*, 2004] and local seismicity analyses [*Béthoux et al.*, 2011]. Quality criterions, related to the station distribution, reduce the number of earthquakes of the MAXI-3D catalog compared to the RENSIG catalog (by about 50% in the offshore domain). The earthquake density map shown in Figure 1b counts the number of earthquakes in cells of 0.09° × 0.09°. The intense seismic activity, offshore the Manta Peninsula and close to La Plata Island, appears even more clearly than in the EHB (Engdahl, van der Hilst, and Buland) catalog [*Engdahl et al.*, 1998] map of Figure 1a.

[7] In the La Plata-Manta region, the abundant seismicity is mostly due to repeated activity, clustered in space and time. In space, this seismicity extends parallel to the trench, covering an 80 km long and 30 km wide area (from the MAXI-3D catalog). In depth, the hypocenters are distributed from the interplate contact zone [from *Graindorge et al.*, 2004] up to the surface [see Figure 8 in *Font et al.*, 2013]. Focal mechanisms of the largest earthquakes of the 1998 and 2005 sequences (from Global Centroid Moment Tensor (GCMT) [*Ekström et al.*, 2012]) exhibit thrust motion (Figure 2). From the hypocenter locations and the associated inverse motion, we infer that past clusters occurred on or close to the subduction interface. In time, these clusters occurred in 1998 [*Segovia*, 2001], 2002, and 2005 [*Segovia*, 2009; *Vaca et al.*, 2009] and lasted from 1 to 3 months (Figure 2). We define these three periods as earthquake swarms as they match the criterions proposed by *Holtkamp and Brudzinski* [2011]: The seismicity rate increase is not related to a clear triggering main shock, several earthquakes have a magnitude close to the largest earthquake of the cluster, and the activity of the cluster terminates abruptly. The 2005 episode was the largest of these swarms, with 485 events with magnitude ML larger than 4, among which four main shocks have a moment magnitude between 6 and 6.2 (Figure 2) [*Vaca et al.*, 2009]. The 2005 seismic swarm has also been detected at the global scale, as 43 earthquakes were located by the National Earthquake Information Center (NEIC) (with a magnitude threshold of 4–4.5) in January–February 2005 [*Holtkamp and Brudzinski*, 2011; *Holtkamp et al.*, 2011]. In this area, these last two studies also point out a smaller swarm in 1977.

[8] Since the end of 2008, the Ecuadorian coast is continuously monitored by an array of nine stations including on each site a GPS equipment (recording at 5 Hz), a broadband seismometer, and an accelerometer (Andes du Nord "ADN" project; Figure 1). This French-Ecuadorian project has been built in collaboration with the IG-EPN and the French laboratory of Geoazur. The new instrumentation, together with the stations of the IG-EPN seismic and GPS networks, allows us to monitor a broad range of processes acting in a subduction zone, including tectonic deformation, aseismic movements, or large earthquakes. During the last 3 years, it has also helped to better image the interseismic coupling along the subduction interface. To determine its spatial distribution, we have used a combination of the continuous

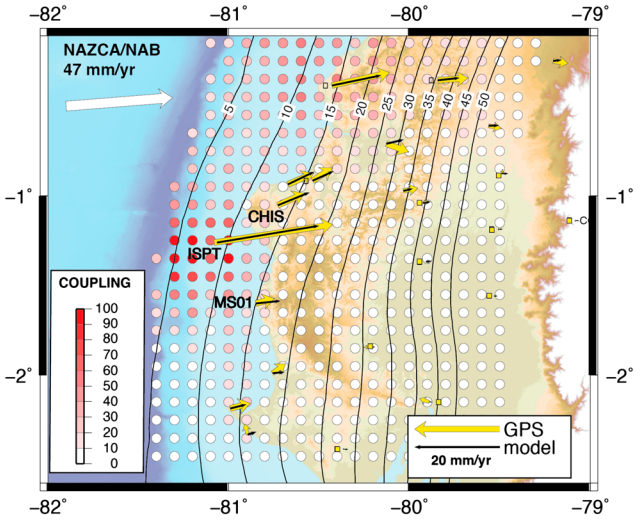

Figure 3. Map of spatial distribution of coupling along the Central Ecuador subduction zone. The yellow arrows show observed GPS velocities derived from both continuous and campaign measurements. Velocities are expressed with respect to the North Andean Block (NAB). Locations of GPS sites with small velocities are shown by the yellow squares. The three stations discussed in the text (ISPT, CHIS, and MS01) and the isodepth of the subduction interface are indicated on the map [from *Graindorge et al.*, 2004; *Font et al.*, 2013]. The modeled velocities (black arrows) correspond to the optimal spatial distribution of coupling along the subduction interface shown by the color circles. Circle color indicates the level of coupling (see color scale).

GPS stations progressively installed since 2008 and campaign data observed since 1994. The full description of the processing strategy as well as a detailed analysis of the interseismic coupling along the Ecuadorian subduction zone will be described in separate studies. For the purpose of this study, we focus here on the interseismic coupling around the segment of La Plata Island before the 2010 SSE.

[9] When expressed in a stable South America reference frame, velocities in southern Ecuador show the contribution of crustal tectonics and elastic deformation induced by the interseismic locking along part of the subduction interface. In order to separate the two contributions, we take advantage of low coupling observed in southern Ecuador (around latitude 2°S) where GPS sites behave rigidly at the millimeter per year level. In particular, no shortening in the east-west direction is detected, and the velocities are consistent with the ones observed in southern Colombia (International GNSS Service (IGS) site BOGT). Such a motion represents the motion of the North Andean Block (NAB) as introduced by previous studies [*Pennington*, 1981; *Gutscher et al.*, 1999; *Trenkamp et al.*, 2002; *White et al.*, 2003]. It is equivalent to a constant translation motion of 9.5 mm/yr in a 75°N–80°N direction for southern Ecuador which is about twice faster and more eastward oriented than what was previously proposed. Residual velocities with respect to the North Andean Block, presented in Figure 3, are then inverted to determine the elastic locking along the subduction interface.

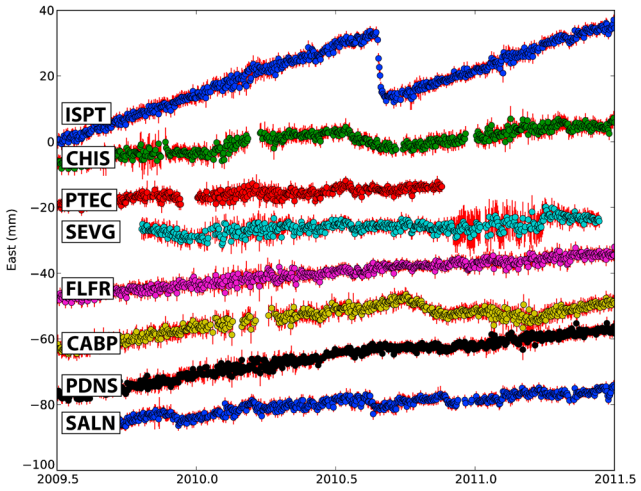

Figure 4. Continuous GPS time series (east component) for the 2009.5–2011.5 period. Formal errors are shown by red lines (1 sigma confidence level). Daily positions (circles) are with respect to the North Andean Block. Clear reversal of the interseismic deformation is observed during 6 days at ISPT, during summer 2010.

[10] We use the back slip approach introduced by *Savage* [1983] to invert for the interplate coupling along the subduction interface, as it was recently done in various other South America subduction zones [*Ruegg et al*., 2009; *Bejar-Pizarro et al*., 2010; *Moreno et al*., 2010; *Chlieh et al*., 2011; *Métois et al*., 2012]. The back slip approach has been shown to be a good approximation, even in the case of nonplanar geometry [*Kanda and Simons*, 2010]. The modeled megathrust surface follows the curved slab geometry proposed by *Font et al*. [2013] based on the background microseismicity and results from marine surveys in the area of La Plata Island [*Graindorge et al*., 2004]. The use of a curved geometry rather than a simple single-plane fault model is justified by the fact that a very shallow dipping subduction interface (~5°) is observed close to the trench [*Graindorge et al*., 2004], with increasing dip further inland, that changes the distance of the GPS sites relative to the subduction interface. It also enables to account for the 25° strike change of the trench axis in the investigated domain. Our fault surface is discretized into 467 elementary subfaults of 11.1 × 11.2 km, covering about 250 km along strike and extending from the trench to 60 km depth. Our model uses a rake fixed to the Nazca/North Andean Block relative motion (Figure 3) and a homogeneous semi-infinite elastic half-space.

[11] Our inversion scheme follows the approach recently described in *Radiguet et al*. [2011], following *Tarantola* [2005], where we minimize the cost function $S(m)$ defined as

$$S(m) = \frac{1}{2}\left[(Gm-d)^t C_d^{-1}(Gm-d) + (m-m_0)^t C_m^{-1}(m-m_0)\right], \quad (1)$$

where m is the unknown parameter model including the amount of back slip for each subfault, m_0 is an a priori model for back slip distribution taken here as 0, and d is the vector of observation including the GPS velocity components. G is the transfer matrix including the contribution of each individual subfault back slip to d. C_d and C_m are the variance-covariance matrices associated with the data and the model, respectively. C_d is taken as a diagonal matrix including the standard deviation derived from the geodetic analysis. C_m is taken in the form of

$$C_m(i,j) = \left(\sigma_m \frac{L}{L_0}\right)^2 \exp\left(-\frac{d(i,j)}{L}\right), \quad (2)$$

where $d(i, j)$ is the distance between two subfaults i and j, L is the critical distance for correlation for slip, and L_0 is a scaling factor fixed at 10 km. The σ_m is taken as the maximum possible velocity (48 mm/yr). We show the results obtained for

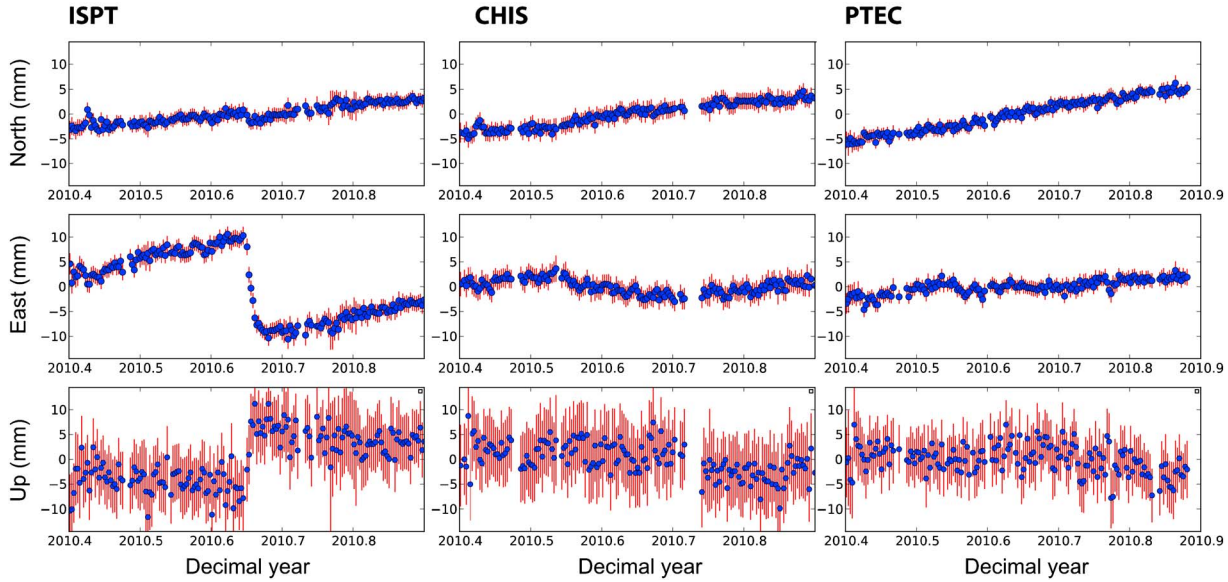

Figure 5. Time series for the three continuous GPS sites used in the search of the SSE parameters. Positions are shown by circles and associated formal errors by red lines (1 sigma confidence level). The SSE is clear on the east and vertical components of ISPT, but its signal is very small on the north component of ISPT, as well as on all the components of CHIS and PTEC.

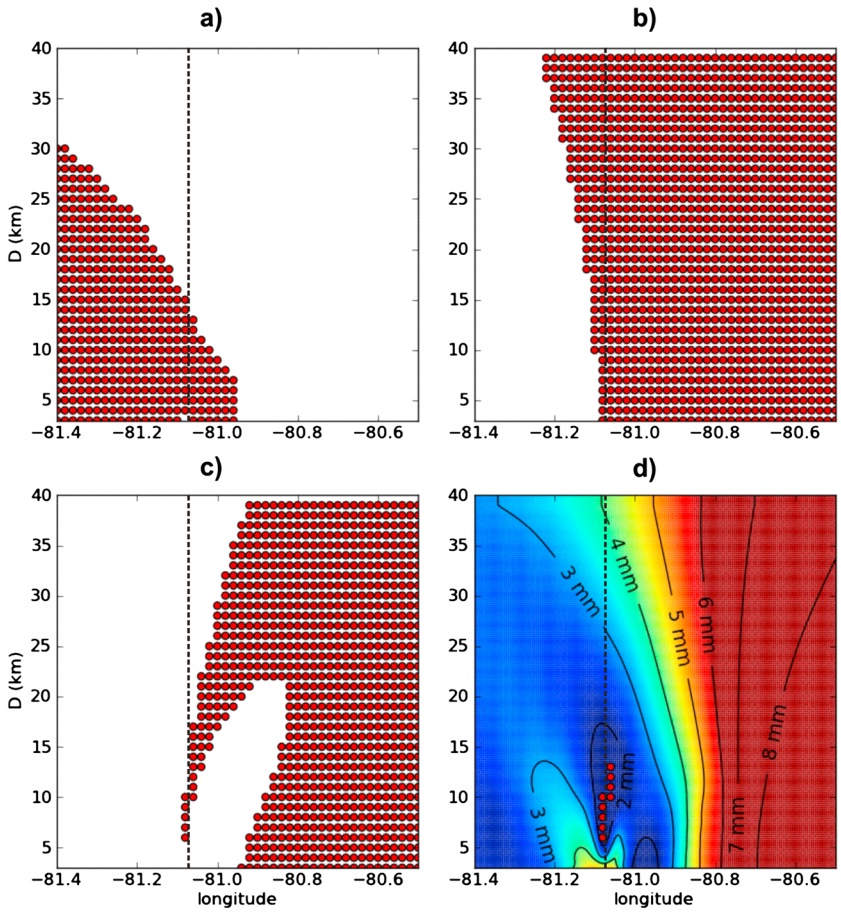

Figure 6. Exploration of the possible spatial parameters of the SSE. All figures show the acceptable models by red dots, in the bidimensional parameter space (λ_0: longitude; D: radius of the slip). The longitude of station ISPT is shown by the vertical dashed line. (a–c) Illustration of how some specific features of the observed displacements forbid some parts of the parameter space (see main text). (d) The location and size of the slow slip patch verifying the three constraints in Figures 6a–6c. Weighted root-mean-square values (in mm) of misfit are shown by the contours and the color scale with increasing values from blue to red.

$L = 50$ km, which is found to be a good value between the roughness of the model and the misfit to the observed GPS velocities.

[12] The inversion reveals the existence of a local (50×50 km) highly coupled area below La Plata Island and extending up to the trench (Figure 3). The high level of coupling is required to explain the velocity of 28.5 ± 0.5 mm/yr at La Plata Island station ISPT. The downdip extension (~15 km) of the locked fault zone is well constrained by the sharply decreasing velocities from ISPT to CHIS (8.8 ± 0.5 mm/yr) and MS01 (5.4 ± 1.5 mm/yr), both located at about 70 km from the trench. Along strike, the extension of the high-coupling area is constrained by the increasing northward component of the velocity at station CHIS and its surrounding. Station MS01 rules out any significant coupling at depth ~15 km at latitude 1.5°S but cannot exclude any significant coupling close to the trench.

3. Slow Slip Observation and Modeling

[13] Figure 4 shows the east component time evolution of the continuous GPS sites expressed in the NAB reference frame. In this framework, the trends of increasing east displacement through time directly witness the elastic effect of interplate coupling along the subduction interface. Time series have been corrected for the common mode network motion [*Wdowinski et al.*, 1997]. They typically have weekly repeatability of the order of 1–2 mm enabling to have a precise monitoring of short-term transient.

[14] At station ISPT, the time series clearly show a ~2 cm rapid progressive westward displacement detected from 26 August 2010, decelerating from 30 August 2010 for a few days, before recovering a constant rate interseismic displacement. Mainly because of the lower precision of the GPS on the vertical component, no clear progressive motion is seen on the vertical component (Figure 5). Nonetheless, we average the position 5 days before and after the SSE and find a total displacement of -19.6 ± 1.1, -2.0 ± 1.0, and 11.25 ± 3.3 mm on the east, north, and upward components, respectively (uncertainties are 1σ confidence interval). During the same period of time, no significant displacement is found neither at the closest station to ISPT, CHIS, nor at PTEC (see the location of the stations in Figure 1 and their three-component displacements in Figure 5).

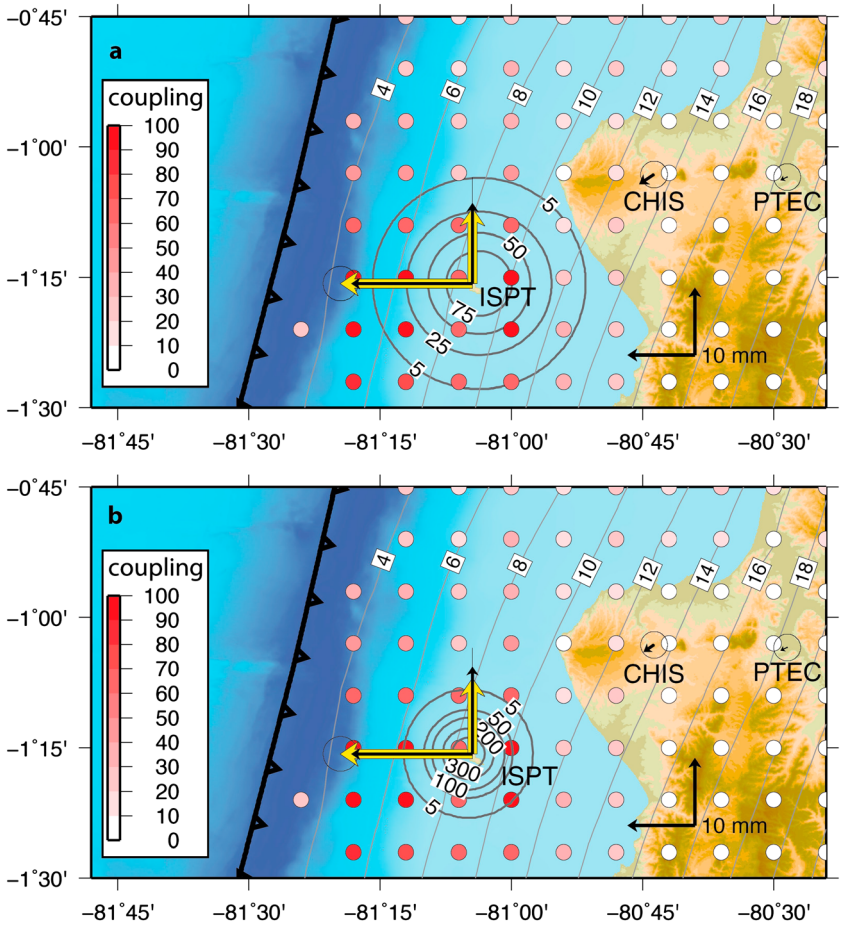

Figure 7. Map view of the two extreme possible slip models. (a) Model corresponding to a characteristic slip radius of 13 km and a maximum slip of ~10 cm. (b) Model corresponding to a characteristic slip radius of 6 km and a maximum slip of ~40 cm. The thick yellow and thin black arrows are observed and modeled displacements, respectively (horizontal and vertical components). Numbers along the concentric circles indicate isovalues of slip (in mm). Depth contours of the subduction interface and coupling spatial distribution are indicated as in Figure 3. Both models indicate that the area of major slip occurred within the deeper part of the area coupled during the interseismic phase, with possible slip extending in the partially coupled area for the extreme model in Figure 7b.

[15] With only one site having significant displacement during the SSE, any proper inversion of the slip distribution is excluded. Nonetheless, we can examine the constraints provided by the data at stations ISPT, CHIS, and PTEC in order to evaluate the range of models able to explain them. In order to reduce the number of parameters to be searched, we use an a priori model of the slip distribution in the bidimensional Gaussian form

$$s(\lambda,\varphi) = s_{\max} \exp\left[-R_t^2\left(\cos^2\varphi_0(\lambda-\lambda_0)^2 + (\varphi-\varphi_0)^2\right)/D^2\right], \quad (3)$$

where s is the slip along the subduction interface at longitude λ and latitude φ (expressed in radians). (λ_0, φ_0) is the location of maximum slip, s_{max} R_t is the radius of the Earth, and D is the characteristic radius of significant slip. The rake is fixed at 90°. We then examine the constraints provided by the total displacement observed at ISPT and the null displacements at the nearby sites CHIS and PTEC (taken at the precision of the GPS, here found to be 1.1 mm on the horizontal components at CHIS and PTEC and 3.9 mm on the vertical component, at the 1σ confidence level).

[16] The first constraint is that very small north component of displacement is found at ISPT. That means that either the motion was homogeneous over a large area surrounding the site ISPT or the slip was at the first order symmetrical either side of the ISPT site. The lack of displacement noticed at CHIS favors the latter hypothesis. The φ_0 was therefore kept fixed to the latitude of ISPT; that is, we search for possible slip distribution models whose center lies along a line going through the location of ISPT in an east-west direction. We sample the model space, by varying λ_0 from the trench (81.4°W) to 80.5°W and varying D from 3 to 40 km. For each (λ_0, D), s_{max} is a simple scaling factor that can be directly estimated using a least squares inversion. Using this formulation, we investigate how the observations constrain the range of possible models (Figure 6).

[17] The absence of any significant displacement detected at CHIS and PTEC excludes any significant amount of slip below the coastline or inland. Figure 6a shows the acceptable region of the parameters space, which meets the criterion of a 2 cm eastward displacement at ISPT and a null displacement at CHIS and PTEC (at the 3σ confidence level). The second constraint is the upward displacement observed at ISPT.

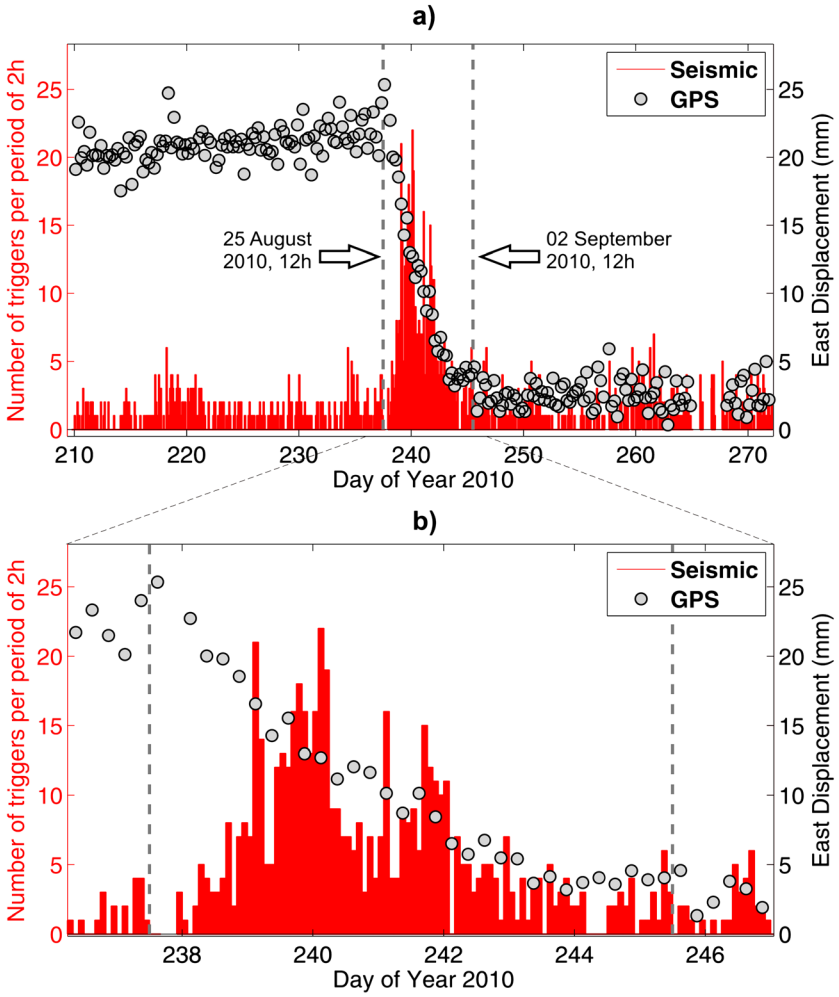

Figure 8. Joint observations of the geodetic displacement and of the seismicity rate at La Plata Island (ISPT station) during the 2010 SSE. Number of seismic events detected over 2 h sessions for an STA/LTA ratio higher than 6.0 (red). East displacement recorded by the GPS station, calculated every 6 h (grey dots). (a) The time window starting 4 weeks before the SSE and ending 4 weeks after the SSE. (b) A zoom detailing seismic activity and geodetic displacement during the SSE. In both figures, the left and right dashed lines indicate the dates of 25 August 2010 (12 h) and 2 September 2010 (12 h), respectively.

Analytic solutions for a 2-D thrust buried dislocation [e.g., *Freund and Barnett*, 1976; *Rani and Singh*, 1992; *Tomar and Dhiman*, 2003; *Cohen*, 1999; *Chlieh et al.*, 2008] indicate that for a buried thrust fault, vertical surface displacements are predicted to be upward on the updip side of the dislocation and downward on the downdip side, the transition between the two regimes occurring above the dislocation. Figure 6b shows the region filling the criterion of upward displacement at ISPT. Taken together, these two constraints limit the range of the possible slip area from about 81.12°W to 80.96°W and a characteristic radius below 18 km. A final constraint is provided by the ratio between the upward and east displacements which is of the order of −0.5. Taking the uncertainties into account, this ratio is considered acceptable in the range [−0.77 −0.38]. Respecting such a ratio range indicates two possible ranges of slip location with respect to ISPT (Figure 6c). One class of models corresponds to slip located in the very near vicinity of ISPT, in agreement with the previous constraints. The second class is obtained for slip located farther east of ISPT, which can be discarded due to the absence of slip observed at station CHIS.

[18] Taking all these constraints into account, we find that the range of possible values is rather narrow: The longitude λ_0 of maximum slip is located between 81.08°W and 81.06°W, and the characteristic slip radius D is in the range [6 km 13 km] (see Figure 6d). For any solution belonging to these intervals, the weighted root-mean-square is below 2 mm, therefore in agreement with the GPS displacements uncertainties. The amount of maximum slip s_{max} is not well resolved, ranging between 97 mm and 407 mm. Moreover, this is a local value that may not be very representative of the global process. Averaged over the area where it is larger than 5% of its maximum, slip is found in the range 50–200 mm. The moment is better resolved and always remains in the range of Mw = 6.0–6.1 (using a classical rigidity of 30 GPa). Figure 7 shows the slip distribution for the two extreme models (λ_0 = 81.06°W, D = 13 km and λ_0 = 81.08°W, D = 6 km).

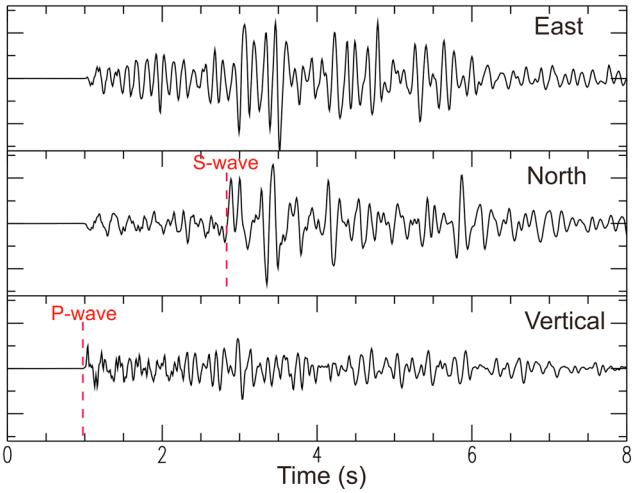

Figure 9. Typical local earthquake waveforms (in velocity) recorded at the ISPT station (origin time of the event: 27 August 2010, 08 h, 57 min, 15 s). The three components are shown at the same scale.

[19] Our parameter search shows that the main area of slip is located close to the downdip limit of the interseismically highly coupled area (Figure 3). Slip extending at greater depth in the partially coupled area is possible for some extreme models, but the range of acceptable radius found in the grid search prevents any further quantification. However, our parameter grid search rules out any slip distribution occurring from the trench to the downdip limit of the locked zone or even any slip distribution centered west of ISPT. In terms of moment release, our search does not account for along-strike extension of the slip. We might therefore underestimate the moment release, as an aspect ratio of 3 would increase the moment magnitude by 0.2–0.3. Taking this into account, the equivalent moment magnitude (Mw) released during the 2010 SSE is found to be in the range of 6.0–6.3.

4. Properties of the Associated Seismicity

4.1. Evidence of Intense Seismic Activity

[20] Visual screening of data recorded at station ISPT shows a rate of seismic events higher than usual during the period of occurrence of the SSE. To quantify this increase of activity, we applied to the continuous data a STA/LTA (Short Term Average over Long Term Average) detection algorithm using a LTA of 60 s and a STA of 1 s. The counting of events detected using this technique is presented in Figure 8, conjointly with the GPS displacements calculated every 6 h. Despite a relatively high background number of detections mainly related to oceanic noise, the curve clearly points out an increase of seismic activity during the SSE. The seismic activity does not start before the beginning of the SSE and thus does not appear to have a role in the SSE initiation. The period of strongest seismic activity (26–29 August) correlates very well with the period of fastest displacement observed at the GPS station. During these 4 days, several distinct peaks in the number of events are visible, showing variations of seismic activity during the SSE itself. Most of the events are not detected at other stations of the ADN array, located about 120 km away for the closest ones (CABP and SEVS; see Figure 1), which indicates that the seismicity is dominated by local and low-magnitude earthquakes.

[21] The visual shape of the waveforms confirms the local character of the seismicity. Most events show clear *P* and *S* arrivals, with a time difference of the order of 1.5–3 s. The impulsive arrivals of the waves do not differ from those of local earthquakes regularly recorded along the Ecuadorian coast. While this "classical" seismicity increase is very clear during the SSE, it also seems that no tremor-like activity has been triggered. Both visual screening of the 7 day long sequence and analysis of the energy variations in successive time windows [*Payero et al.*, 2008] do not indicate peculiar features. Even if some minor tremor activity might be discovered by refined analyses [*Kim et al.*, 2011], it clearly appears that the regular earthquakes with impulsive waves arrival define the main seismic process associated with this SSE.

[22] In the following paragraphs, we therefore concentrate on the properties of this associated seismicity. Two approaches are considered. We first use the three components of the broadband station ISPT to locate and characterize the largest events of the seismic sequence. This reduces the analyzed activity to a total of about 50 events. In a second time, we perform waveform classification based on cross-correlation techniques. Such an approach does not provide the absolute source parameters but has the double advantage of (1) giving a robust estimate of the number of tectonic events (while STA/LTA detection procedure may also identify various technical artifacts) and, more importantly, (2) enlightening how part of the seismicity is organized in terms of repeating events.

4.2. Location and Source Properties of the Largest Events

[23] Because most events are only recorded by station ISPT, we cannot use standard phase picking techniques to locate them. However, the events exhibit clear *P* and *S* wave arrivals, with a small time difference between *P* and *S* waves and a large *P* wave amplitude on the vertical component (Figure 9). This indicates that a large number of earthquakes have an epicenter close to the La Plata Island. We can therefore estimate the earthquakes location by studying the particle motions at the ISPT station [see, e.g., *Alessandrini et al.*, 1994, and references therein]. We first determine the back azimuth of the earthquake by rotating the horizontal components and finding the orientation that minimizes the waveform energy along one of the rotated components. Using this information, we repeat the previous operation with the radial and vertical components to retrieve the incidence angle of the *P* wave (see illustration and more information about this procedure in Supplementary Figure A.1 in the supporting information). Finally, the differential time between *P* and *S* waves allows us to estimate the location of the earthquake along the *P* ray.

Table 1. One-Dimensional Models Used to Locate the Triggered Seismicity

East of ISPT			West of ISPT		
Depth (km)	*P* Velocity (km/s)	*S* Velocity (km/s)	Depth (km)	*P* Velocity (km/s)	*S* Velocity (km/s)
0–2	4.3	2.48	0–5	4.3	2.48
≥2	6	3.46	≥5	6	3.46

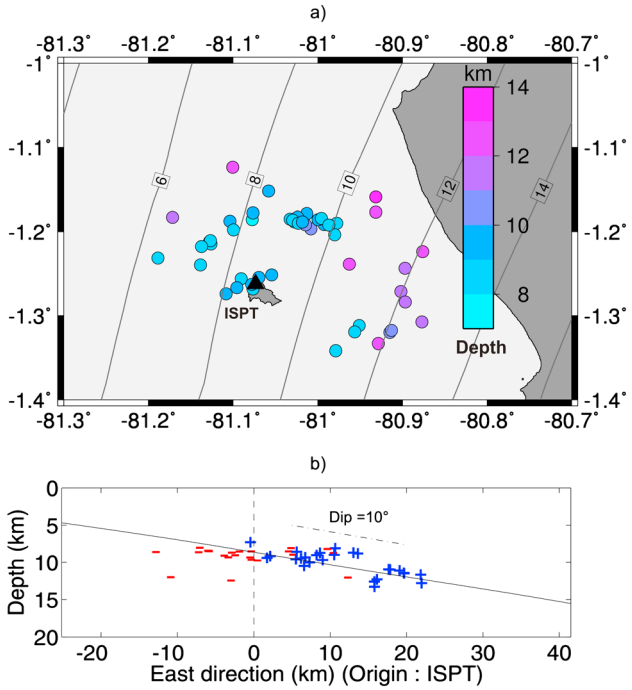

Figure 10. Hypocentral location of the largest events. (a) Map location with color scaled to depth. The annotated contours indicate the depth of the subduction interface as in Figure 3. (b) Projection on the west-east vertical plane. The black line represents the subduction interface. The optimal linear fit of the events east of ISPT defines a 10° dip (dash-dotted line). Polarities on the vertical component of the ISPT broadband station are shown in the cross section.

[24] The variations of the crustal wave velocities add some complexity to this simple approach. In this study, we neglect the effects of the lateral variations and only consider the dominant effects of wave velocities increasing with depth. In this one-dimensional model, the back azimuth determination is not affected. The incidence angle determination is made more difficult, because the radial component includes both the direct *P* wave and *P-S* waves refracted below the station. If using unfiltered signals over a duration including some *P-S* waves, the determination of the incidence angle is biased by these different wave types arriving on the vertical and radial components. If using very short time windows close the first *P* wave arrival, the determination is less stable and only reflects the incidence angle in the very shallow part of the crust. To obtain a more robust value, we band-pass the signal between 1 Hz and 4 Hz and use the first 0.4 s following the *P* wave arrival. Such a filtering reduces the potential number of analyzable earthquakes, because of the low signal-to-noise ratio for small events waveforms low-passed at 4 Hz. Based on amplitude criterions, we finally select 49 earthquakes for which the determination of back azimuth and incidence angles is reliable.

[25] The location of the hypocenter along the *P* ray is more directly dependent on the wave velocity structure. To estimate its realistic variation close the La Plata Island, we use the study of *Graindorge et al.* [2004], who have derived an east-west crustal model by inversion of wide-angle seismic data. This profile is located only 15 km south of La Plata Island and is therefore well adapted to the present study. The depth of interplate seismicity, observed during a seismic experiment (SISTEUR) [*Béthoux et al.*, 2011], was shown to be consistent with the *Graindorge et al.* [2004] model. It reveals that below the La Plata Island, solid crustal rocks ("Piñon" formation, with *P* wave velocities of the order of 6–6.5 km/s) are already present at 2–5 km depth. This is a favorable configuration for the location technique, as the ray geometry of the *P* wave should remain simple between the subduction interface and superficial depths. Based on the

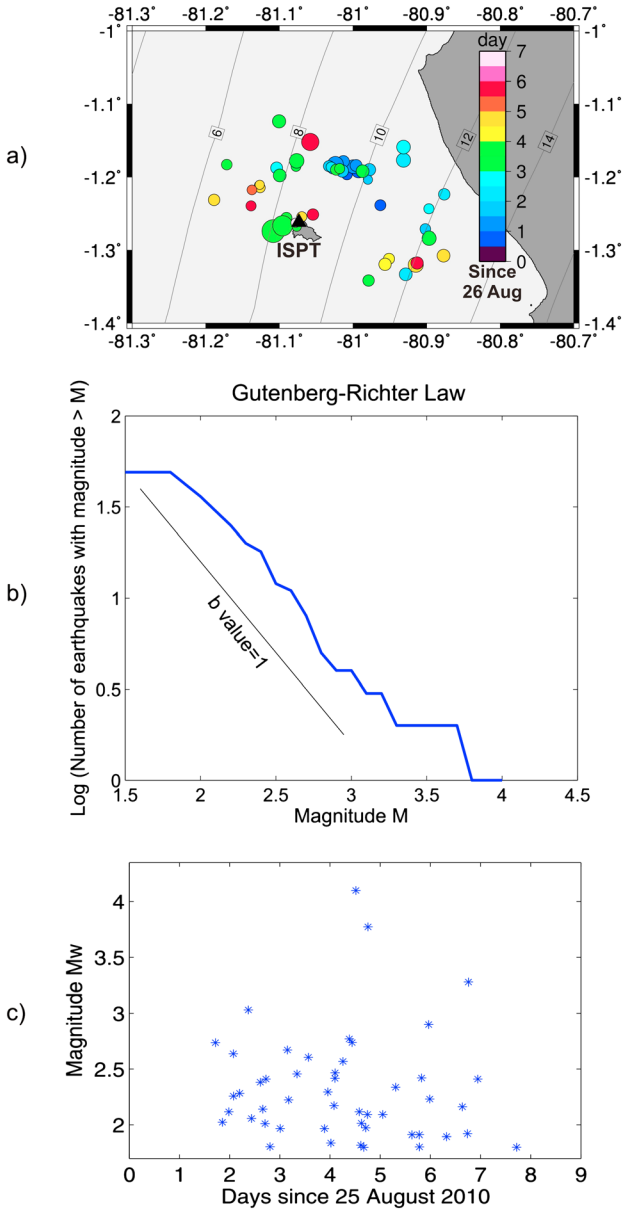

Figure 11. Magnitude and time distribution of the associated seismicity. (a) Map location, with color scaled to occurrence date and size to moment magnitude (Mw). The smallest circles are events of Mw = 1.8, and the largest one is a Mw = 4.1 earthquake. The depth of the subduction interface is contoured and labeled (in km) as in Figure 3. (b) Gutenberg-Richter law with the classical b-value slope (equal to 1) presented on the left part of the figure. (c) Distribution of magnitude as a function of occurrence time.

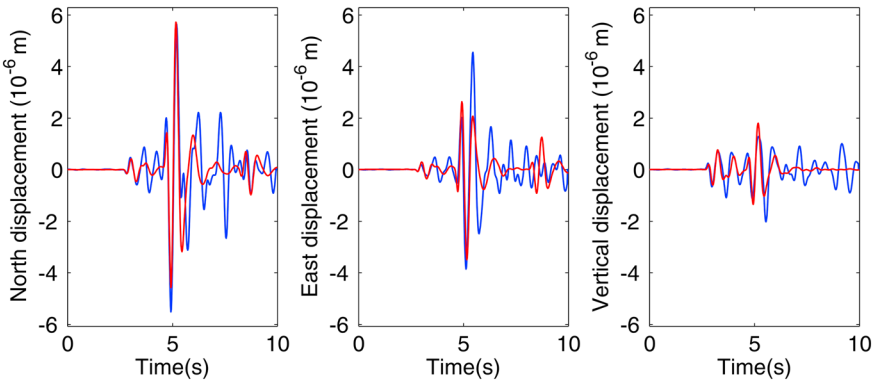

Figure 12. Comparison between displacements recorded at the ISPT station (blue) and synthetics (red), for the 27 August 2010, 08 h, 57 min, 15 s, event (see raw data in Figure 9). Both data and synthetics are band-pass filtered between 1 Hz and 2.5 Hz. This earthquake has been located at (latitude, longitude, depth) = (1.19°S, 81.02°W, 9.5 km) by the location procedure. The source parameters corresponding to synthetics are (strike, dip, rake) = (13°, 9°, 80°) and Mw = 3. The good agreement between data and synthetics shows that this earthquake is consistent with a thrust mechanism along the subduction interface.

Graindorge et al. [2004] model, we derive two average layered models (presented in Table 1) to take into account that the top of the Piñon formation is deeper west of ISPT. Depending on the back azimuth, we select the corresponding model to locate the hypocenter along the *P* ray using the differential *S-P* time.

[26] In Figure 10, we present the obtained hypocentral locations, both in map and projected along a west-east vertical plane. The depth locations for earthquakes located below ISPT (8–10 km) are in good agreement with the depth of the subduction interface determined by *Graindorge et al*. [2004]. These depths are little affected if using different realistic velocity values for the first layer, because the ray is almost vertical. Depths for earthquakes east of ISPT are more sensitive to the first layer parameters, as faster velocities inside this first layer lead to steeper rays, then resulting in deeper hypocenters. However, all models result in an increasing depth for earthquakes located more inland, in agreement with events occurring on or close to the subduction interface. Using the model presented in Table 1, the best average dip east of ISPT is found to be equal to 10°, the same value as in the *Graindorge et al*. [2004] model. In Figure 10b, we add to the depth location the polarities read on the vertical component of the ISPT station. As expected, for thrust earthquakes occurring on an almost flat interface, most polarities are positive east of ISPT and negative west of ISPT. These elements are consistent with a typical release of the stress accumulated during the interseismic period.

[27] The magnitude distribution can be estimated by modeling the waveforms of the earthquakes. We invert the waveforms—filtered in the [1 Hz 2.5 Hz] range—to retrieve the mechanism and moment magnitude, using a window starting at the *P* wave arrival and ending 1 s after the *S* wave. To do so, we have developed an inversion scheme based on the wavefield modeling by the discrete wave number method [*Bouchon*, 1981]. The mechanism determination may be ambiguous, but the magnitude is expected to remain meaningful. Figure 11a shows the location map of the associated seismicity, with circle sizes scaled to the moment magnitude and colors depending on the occurrence date. We observe that the seismicity started on 26 August close to 81°W, 1.2°S, before migrating, mostly west and south, in the following days. When analyzing the classical magnitude scaling laws (Figures 11b and 11c), we note that the Gutenberg-Richter law is well respected with a classical b-value close to 1. On the other hand, Figure 11c shows that the seismicity does not follow a main shock-aftershock behavior (Omori's law): Large- and small-magnitude events appear to occur randomly, with the largest shocks (Mw = 3.8 and 4.1) occurring on 29 August, several days after the beginning of the sequence. This observation is a further evidence that the seismicity is driven by an external cause—here the SSE—and not by internal stress interaction.

[28] As the focal mechanism may be unreliably retrieved by the analysis of only one seismic station, we adopt a different strategy to further check that the seismicity is consistent with a thrusting mechanism along the interface: In the inversion process, we restrain the possible range of focal mechanism angles (in such a way that only realistic interface thrust earthquakes can be modeled) and evaluate if the real waveforms can be adequately matched. We present in Figure 12 an example of waveforms modeling (the same earthquake as in Figure 9), illustrating that *P* and *S* waves are satisfactorily modeled, on the three components, by a typical subduction mechanism. For the earthquakes with Mw > 2.5, we found that 9 earthquakes over 12 have both their polarities and waveforms in agreement with inverse slip on the subduction interface.

[29] As shown in Figure 11, the largest events of the sequence are two earthquakes of moment magnitude equal to 3.8 and 4.1. We estimate the cumulated moment released by the smaller earthquakes by integrating the Gutenberg-Richter law [see *Andrews and Schwerer*, 2000] and obtain an equivalent moment magnitude of 3.7. As a whole, the seismicity released a seismic moment equivalent to a Mw = 4.2 earthquake, much smaller than the moment magnitude of the SSE (Mw larger than 6.0). In terms of moment ratio, the cumulative moment released through earthquakes accounts for 0.1–0.2% of the total moment release. Together with the location, timing, and mechanism analysis, this observation is fully consistent with a slip on the subduction interface mostly accommodated by the SSE, which has

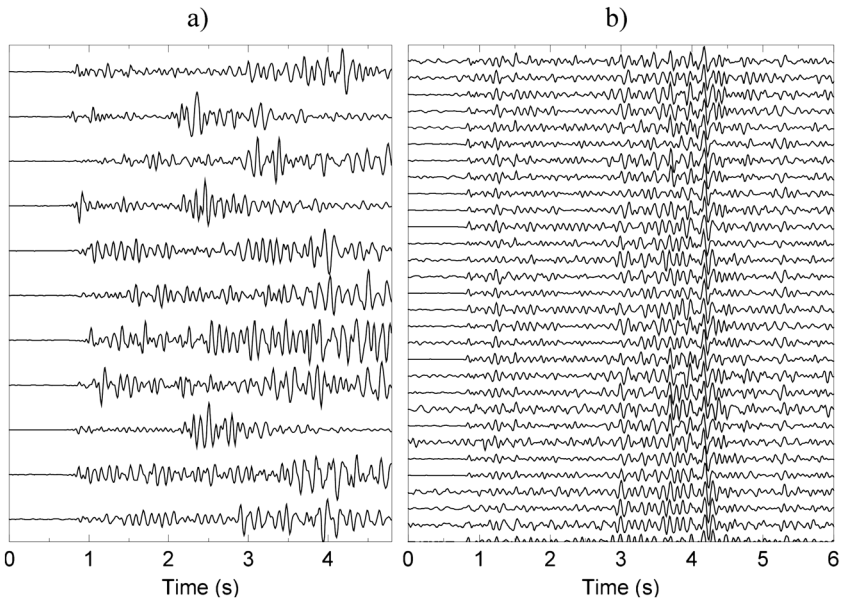

Figure 13. (a) Examples of reference stacks used to scan the data. (b) Examples of similar waveforms detected for the largest family active during the SSE.

itself seismically triggered small locked patches, located on or very close to the interface. To better characterize the behavior of these locked patches, we now specifically analyze how the whole triggered seismicity (and not only the largest earthquakes) is organized in terms of repeating events.

4.3. Organization of the Seismicity

[30] We now select all triggers with a STA/LTA higher than 4.0 between 28 July and 6 October 2010 and, in addition, those with a STA/LTA between 3.0 and 4.0 between 25 August and 2 September 2010. The choice of such low detection thresholds enables the detection of small-amplitude events but has the drawback of also selecting numerous noisy traces that will be disregarded later in the processing. For the 8971 triggers, we extracted for the vertical component of ISPT windows with a 2048-sample (16.4 s) length starting 500 samples (4 s) before the triggering times. All waveforms have been compared one to each other using cross correlation after filtering between 3 and 17 Hz. We consider that an event belongs to a family if it has a correlation higher than 0.80 with at least one of the other events. The classification indicates the presence of 34 families of similar tectonic earthquakes (Figure 13) including more than five events and grouping a total of 270 earthquakes. Thirty of these families only include events which occurred during the SSE. Additionally, 406 earthquakes are grouped into smaller families of less than five events. This procedure allows the determination of the main active clusters during the SSE and during the few months around. The similarity of waveforms guaranties that events belonging to the same family have both similar hypocentral locations and source characteristics.

[31] To recover precisely the time history of the 34 largest families over a duration longer than that of the SSE, as well as to identify events possibly missed in the detection or in the classification, we scan the data using a matched-filter technique. We generate for each family a synthetic waveform of 600 samples (4.8 s) obtained by stacking all similar events (Figure 13). These waveforms, calculated for the vertical component of ISPT, include for most of them both *P* and *S* phases indicating hypocentral distances between 10 and 20 km. The stacks are used to scan the data by sliding the reference waveforms along the continuous data in search of similar signal windows. The scanning is performed after band-pass filtering both the reference traces and the continuous data between

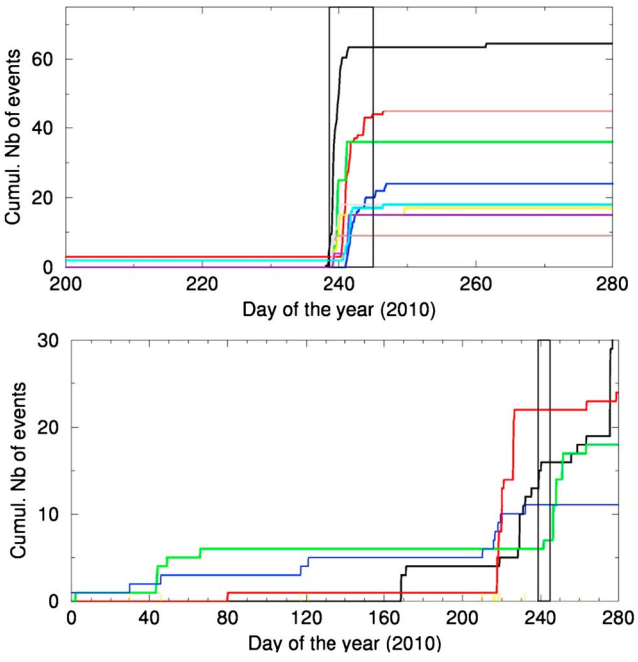

Figure 14. (top) For the 10 largest families active during the SSE, the cumulated number of events detected since 8 July 2009. (bottom) Similar cumulated numbers for families active during months around the SSE. In both plots, the period of activity of the SSE is between the two vertical black lines.

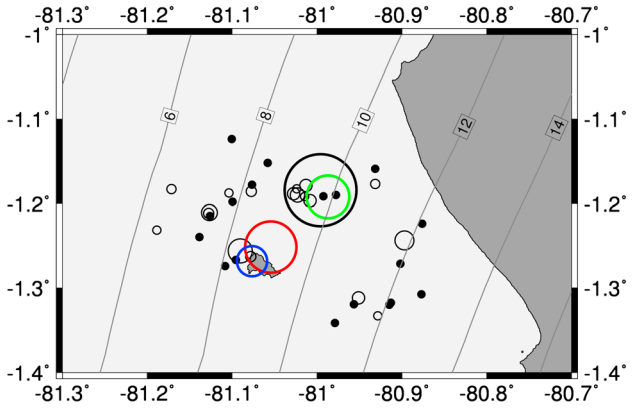

Figure 15. Family character of the located seismicity. The circle diameters are scaled to the number of events similar to the located earthquake. The four largest families (including, respectively, 65, 45, 36, and 24 events) are contoured with the same colors as in Figure 14 and give the scale to the family population. Black dots show individual events, and the smallest empty circles are doublets. The depth of the subduction interface is contoured and labeled (in km) as in Figure 3.

3 and 17 Hz. We analyze the entire period from 8 July 2009 to 6 October 2010. To detect a maximum number of events similar to the reference stacks, we consider as similar each time window with a cross correlation higher than 0.7. The procedure now allows us to significantly increase the number of events involved in each family, since, for the chosen correlation threshold, 573 events are now involved in the 34 main clusters. For 30 of the families, temporal distributions are similar to those shown in Figure 14 (top), with most of the events occurring only during the SSE. On the contrary, the four remaining clusters are active indifferently of the occurrence of the SSE. This result shows that specific seismogenic structures are activated only during the SSE.

[32] Comparing with the 49 earthquakes located in section 4.2, we directly find that 11 of these larger earthquakes belong to one of the 30 main families. Two pairs of located earthquakes belong to a same family, which informs us on the internal quality of the location procedure: We find that the locations differ by about 1 km for earthquakes belonging to the same family. Using again the matched-filter technique, we further check if some of these larger earthquakes are really orphans or if the occurrence of repeating similar events is the rule for this triggered seismicity (Figure 15). We find that 23 earthquakes

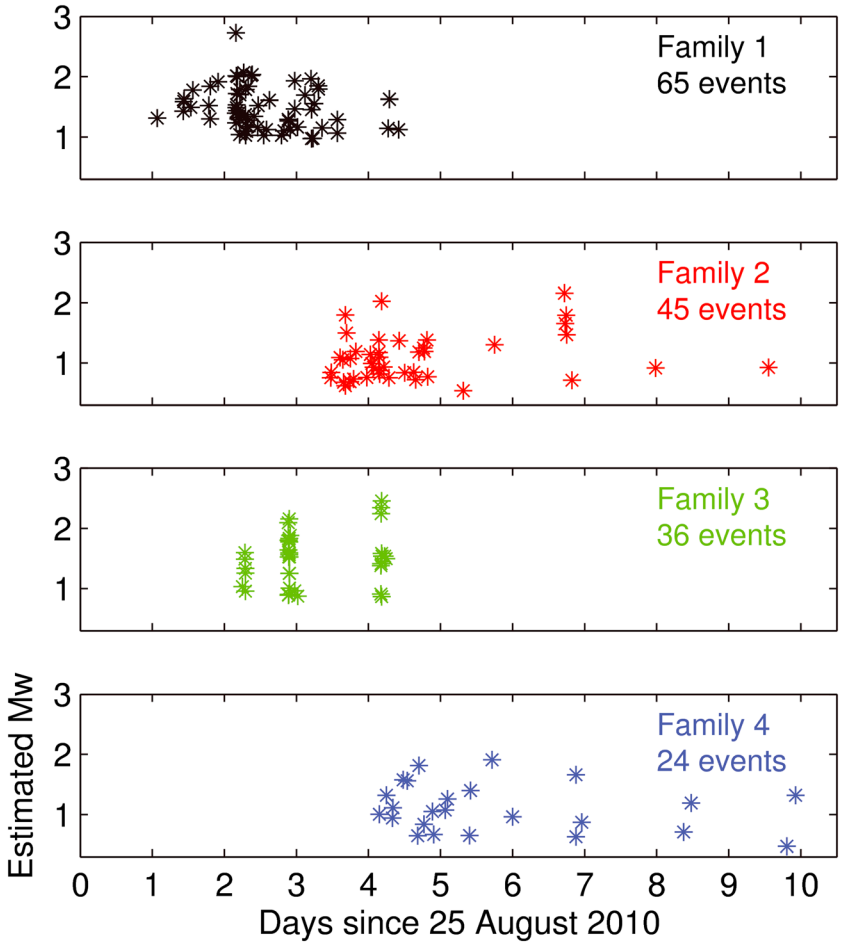

Figure 16. Temporal activation of the four main seismicity families. The moment magnitude (Mw; vertical scale) has been derived using the amplitude ratio between each event and the larger event of the family, for which we have an independent estimate of the magnitude (see section 4.2).

cannot be associated with more than one event. The six largest earthquakes (with Mw larger than or equal to 2.8) belong to this group in which events occur as singlets or doublets. The other earthquakes present a repeating character, which can be moderate (10 earthquakes can be integrated in families of less than 10 events) or very active: Four earthquakes belong to families of more than 20 events (colored circles in Figure 15), the largest one grouping 65 events (see also Figure 14). These observations show that the SSE triggers different types of seismicity. Part of it can be understood as immediate stress release on locked patches of the interface, resulting in orphan events. The largest earthquakes belong to this category and illustrate the triggering potential of SSE for large interplate earthquakes. The events grouped into families indicate that the stress release on some areas of the interface is more complex, with the conjugate effect of SSE stress loading and earthquake interaction. We present in Figure 16 the temporal activation of the four main families. As for the whole sequence, the magnitude occurrence inside each family as a function of time does not follow a simple law. This observation suggests that the time-dependent stress induced by the SSE is the dominant triggering factor and that a small seismogenic area progressively ruptures as stress increases with time. However, earthquake interaction also plays a role in the seismicity rate inside a family. This is clear for family 1, where higher seismic activity is present just after the largest earthquake of this family (Figure 16).

5. Discussion and Conclusions

5.1. SSE Scaling Laws

[33] The increasing number of SSEs observed in several subduction zones has offered the possibility to examine their scaling relations [*Ide et al*., 2007; *Peng and Gomberg*, 2010; *Gao et al*., 2012]. These studies have enlightened the fact that the moment released during SSEs appears to be proportional to their duration, which differs from the earthquakes behavior where seismic moment grows as the cube of the duration. In this respect, the Central Ecuador SSE (Mw = 6.0–6.3 associated with a duration of 6–7 days) is well aligned with the trend observed by *Ide et al*. [2007].

[34] On the other hand, the slip extension appears to be more compact than that for the other documented SSEs. This characteristic is directly related to static stress drop, which can be estimated from any coseismic slip distribution using the formalism of *Sato* [1972] [see also *Singh*, 1977]. When using the Gaussian model of equation (3), together with a characteristic dimension R of the SSE, average stress drop can therefore be determined. We use a value for R equal to $1.25D$ (D is defined in equation (3)). In this case, 79% of the moment is included inside the disc of radius R. Considering the extreme values for D (6 km–13 km) and $s_{\max}$ (10 cm–40 cm) determined in section 3, we find that stress drop is in the range 0.07–0.7 MPa. These values are not abnormal for earthquakes but are significantly larger than the ones observed for SSEs, which are typically of the order of 0.0001–0.01 MPa [*Gao et al*., 2012]. This suggests that some classes of SSEs may share some of the characteristics of earthquakes, which differs from the conclusions of *Ide et al*. [2007]. As a matter of fact, these authors propose that slow and rapid processes have completely distinct behaviors. Our observation rather supports a larger diversity in the scaling laws of the deformation processes, in better agreement with the study of *Peng and Gomberg* [2010].

5.2. Relations Between Slow Slip and Seismicity

[35] This study provides some striking evidence of the seismic triggering potential of slow slip processes. This causality has been observed in other subduction zones (Hikurangi, New Zealand; Boso Peninsula, Japan; and Guerrero, Mexico) but with less accuracy on the spatiotemporal properties relating the two phenomena. It has also been suggested based only on abnormal characteristics of the seismicity [*Holtkamp and Brudzinski*, 2011; *Holtkamp et al*., 2011; *Kato et al*., 2012; *Bouchon et al*., 2011]. Our study strongly supports that a peculiar behavior of the seismicity, expressed by swarms or repeated events, may find its origin in a slow slip process.

[36] Figure 17 shows the spatial distribution of the slow slip and of its associated seismicity. It reveals that most of the seismicity occurred inside or very close to the zone affected by the slow slip. In other words, the spatial extension of the seismic crisis is a good first-order evaluation of the size and location of the SSE. This was not the case for seismicity associated to other SSEs (Hikurangi, New Zealand [*Delahaye et al*., 2009]; Boso Peninsula, Japan [*Sagiya*, 2004]; and Guerrero, Mexico [*Liu et al*., 2007]), where the earthquakes were adjacent to the slow slip area. In particular, slow slip and seismicity are both shown to be active below La Plata Island. Two interpretations may account for this observation. This can be explained by a mostly aseismic subduction interface, over which small and localized patches break seismically. However, since earthquakes have a magnitude lower than ~4, most of them accommodate a displacement well below the centimeter level, if we assume classical seismic scaling laws to be valid. Thus, the seismic slip for a given patch should still be small compared to its full motion during the SSE. This, in turn, implies that the seismic patches should have themselves a mixed behavior, partitioned between seismic and aseismic processes, to be consistent with several centimeters of slip on the plate interface. Alternatively, the seismicity may have occurred on small structures, surrounding the main subduction interface where the slow slip developed. Small faults connected to the interface, directly above or below it, would be candidates for this associated seismicity.

[37] Both interpretations imply that seismicity is intimately related to the slow slip process. This offers a way to derive some spatiotemporal characteristics of the SSE by tracking the characteristics of the seismicity. In particular, rupture velocity of the SSE can be evaluated by the location and occurrence time of the earthquakes. When looking at the 49 located earthquakes, propagation from northeast to southwest is visible; however, this tendency shows a large scatter, probably because, at a given location, earthquakes may occur some hours or days after the activation of the slow slip (as shown by the temporal distribution of the main families; Figure 16). Therefore, rupture velocity can be better determined by the location and activation initiation of families of repeating earthquakes rather than by the temporal evolution of seismicity itself. Using this hypothesis for the four main families, we evaluate the rupture velocity of the SSE as 5–7 km/d. This value is consistent with other slow slip processes compiled by *Gao et al*. [2012].

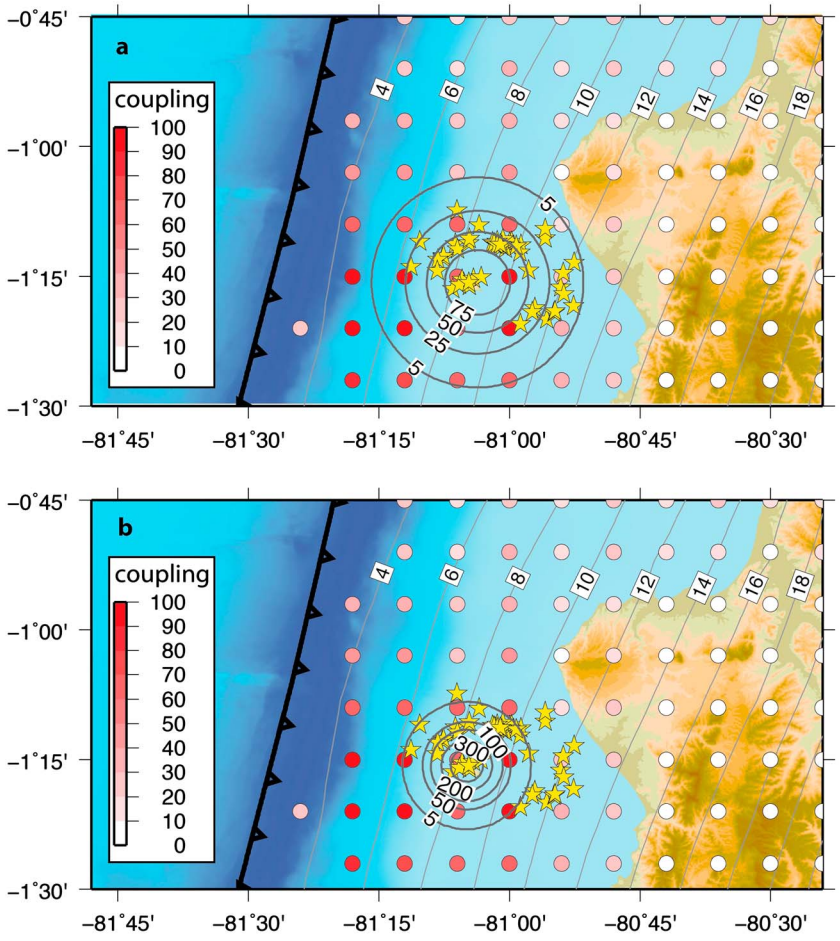

Figure 17. Map view of the slow slip models as in Figure 7 together with the observed seismicity during the SSE. Epicenters are shown by yellow stars. Numbers along the concentric circles indicate isovalues of slip (in mm) as in Figure 7. Depth contours of the subduction interface and coupling spatial distribution are indicated as in Figures 3 and 7. (a) In this case, which corresponds to the upper bound of the slow slip spatial extension, all the seismicity is located inside the slow slip area. (b) In this case, which corresponds to the lower bound of the slow slip area, only the easternmost events are located outside the slow slip area.

[38] This well-documented case may be used as a typical example when simulating, numerically or analogically, the coexistence of slow and rapid deformation processes. We show that the slow slip event has activated seismicity that represents no more than a few tenths of percent of the global deformation (in terms of released moment). Moreover, we show that this seismicity is not homogeneously distributed in space and time. Some localized zones are the loci of an intense seismic activity, as evidenced by the families of repeating earthquakes. These elements may be compared with laboratory experiments, as the one of *Lengliné et al.* [2012]. Reciprocally, if experiments are able to reproduce these observed properties, we should gain information on the frictional characteristics of the subduction interface.

5.3. Seismic Cycle and SSEs in Central Ecuador

[39] Along the subduction segment in the vicinity of the La Plata Island, the coexistence of slow slip processes and seismicity has likely already occurred repeatedly in the past. Since the installation of station ISPT at the end of 2008, geodetic measurements have not revealed any other clear transient signal. Before this date, seismicity remains the best indicator of occurrence of similar episode of deformation. In this respect, the three swarms of 1998, 2002, and 2005 are obvious candidates (Figure 2). If referring to their larger spatial extension, to their longer duration (month(s) instead of 1 week), and to their larger cumulated seismic moment (Mw ~ 6.5 for the 2005 swarm, compared to Mw ~ 4.2 for the 2010 swarm), we suggest that this seismicity originated from larger-scale SSEs. The SSE potentially related to the strong 2005 swarm has not been detected by the interferometric synthetic aperture radar analysis (INSAR) of *Holtkamp et al.* [2011], but as explained by these authors, this is mainly due to the loss of coherence of satellite images.

[40] Frequent SSEs should reduce the size and/or postpone the occurrence of an earthquake breaking the coupled patch below La Plata Island (Figure 3). Seismic swarms thus appear to be a detectable part of larger-scale phenomena, which, in turn, play a significant role in the seismic cycle. Their detection should then be a specific goal of seismic networks. While this detection is sometimes possible at teleseismic distances, local networks are required for an exhaustive analysis. In the specific case of Central Ecuador, future swarm activity

should be better monitored, as five offshore seismometers ocean bottom seismometer (OBS) have been deployed close to the trench and associated with six on-land seismometers installed on the Manta promontory.

[41] **Acknowledgments.** We are grateful to the IRD (Institut de Recherche pour le Développement), the ANR (Agence Nationale de la Recherche; contract ANR-07-BLAN-0143-01), and the IG-EPN for the strong support to the project of instrumentation of the Ecuadorian coast ("ADN" project). On the Ecuadorian side, support was available from the Secretaría Nacional de Educación Superior, Ciencia y Tecnología SENESCYT (Proyecto PIN_08-EPNGEO-00001). The installation and maintenance of the seismic and geodetic arrays would not have been possible without the help of numerous colleagues from the IG-EPN. This study also benefits from the local seismicity catalog of the IG-EPN (RENSIG catalog). We thank F. Hirose and an anonymous reviewer for their constructive comments which helped us to improve the initial manuscript. The careful reading of the Associate Editor was also helpful. Some figures of this article have been drawn using the GMT software (http://gmt.soest.hawaii.edu/).

References

Alessandrini, B., M. Cattaneo, M. Demartin, M. Gasperini, and V. Lanza (1994), A simple P-wave polarization analysis: Its application to earthquake location, *Ann. Geophys.*, *5*, 883–897.

Andrews, D. J., and E. Schwerer (2000), Probability of rupture of multiple fault segments, *Bull. Seismol. Soc. Am.*, *90*, 1498–1506.

Beck, S., and L. Ruff (1984), The rupture process of the great 1979 Colombia earthquake: Evidence from the asperity model, *J. Geophys. Res.*, *89*, 9281–9291.

Bejar-Pizarro, M., et al. (2010), Asperities and barriers on the seismogenic zone in North Chile: State-of-the-art after the 2007 Mw 7.7 Tocopilla earthquake inferred by GPS and InSAR data, *Geophys. J. Int.*, *183*, 390–406, doi:10.1111/j.1365-246X.2010.04748.x.

Béthoux, N., M. Segovia, V. Alvarez, J. Y. Collot, P. Charvis, A. Gailler, and T. Monfret (2011), Seismological study of the central Ecuadorian margin: Evidence of upper plate deformation, *J. South Am. Earth Sci.*, *31*, 139–152.

Bilek, S. L. (2010), Seismicity along the South American subduction zone: Review of large earthquakes, tsunamis, and subduction zone complexity, *Tectonophysics*, *495*, 2–14.

Bouchon, M. (1981), A simple method to calculate Green's functions for elastic layered media, *Bull. Seismol. Soc. Am.*, *71*, 959–971.

Bouchon, M., H. Karabulut, M. Aktar, S. Özalaybey, J. Schmittbuhl, and M. P. Bouin (2011), Extended nucleation of the 1999 M-w 7.6 Izmit earthquake, *Science*, *331*, 877–880.

Chlieh, M., J. P. Avouac, K. Sieh, D. H. Natawidjaja, and J. Galetzka (2008), Heterogeneous coupling of the Sumatran megathrust constrained by geodetic and paleogeodetic measurements, *J. Geophys. Res.*, *113*, B05305, doi:10.1029/2007JB004981.

Chlieh, M., H. Perfettini, H. Tavera, J.-P. Avouac, D. Remy, J.-M. Nocquet, F. Rolandone, F. Bondoux, G. Gabalda, and S. Bonvalot (2011), Interseismic coupling and seismic potential along the Central Andes subduction zone, *J. Geophys. Res.*, *116*, B12405, doi:10.1029/2010JB008166.

Cohen, S. C. (1999), Numerical models of crustal deformation in seismic zones, *Adv. Geophys.*, *41*, 133–231.

Delahaye, E. J., J. Townend, M. E. Reyners, and G. Rogers (2009), Microseismicity but no tremor accompanying slow slip in the Hikurangi subduction zone, New Zealand, *Earth Planet. Sci. Lett.*, *277*, 21–28.

Dorbath, L., A. Cisternas, and C. Dorbath (1990), Assessment of the size of large and great historical earthquakes in Peru, *Bull. Seismol. Soc. Am.*, *80*, 551–576.

Douglas, A., J. Beavan, L. Wallace, and J. Townend (2005), Slow slip on the northern Hikurangi subduction interface, New Zealand, *Geophys. Res. Lett.*, *32*, L16305, doi:10.1029/2005GL023607.

Dragert, H., K. Wang, and T. S. James (2001), A silent slip event on the deeper Cascadia subduction interface, *Science*, *292*, 1525–1528.

Ekström, G., M. Nettles, and A. M. Dziewonski (2012), The Global CMT project 2004–2010: Centroid-moment tensors for 13,017 earthquakes, *Phys. Earth Planet. Inter.*, *200–201*, 1–9.

Engdahl, E. R., and A. Villaseñor (2002), Global seismicity: 1900–1999, in *International Handbook of Earthquake and Engineering Seismology*, part A, chap. 41, edited by W. H. K. Kanamori, P. C. Jennings, and C. Kisslinger, pp. 665–690, Academic Press.

Engdahl, E. R., R. van der Hilst, and R. Buland (1998), Global teleseismic earthquake relocation with improved travel times and procedures for depth determination, *Bull. Seismol. Soc. Am.*, *88*, 722–743.

Font, Y., H. Kao, S. Lallemand, C.-S. Liu, and L.-Y. Chiao (2004), Hypocentre determination offshore of eastern Taiwan using the maximum intersection method, *Geophys. J. Int.*, *158*, 655–675.

Font, Y., M. Segovia, S. Vaca, and T. Theunissen (2013), Seismicity pattern along the Ecuadorian subduction zone: New constraints from earthquake location in a 3D a priori velocity model, *Geophys. J. Int.*, *193*, 263–286, doi:10.1093/gji/ggs083.

Freund, L. B., and D. M. Barnett (1976), A two dimensional analysis of surface deformation due to dip-slip faulting, *Bull. Seismol. Soc. Am.*, *66*, 667–675.

Gao, H., D. A. Schmidt, and R. Weldon (2012), Scaling relationships of source parameters for slow slip events, *Bull. Seismol. Soc. Am.*, *102*, 352–360.

Graindorge, D., A. Calahorrano, P. Charvis, J.-Y. Collot, and N. Béthoux (2004), Deep structures of the Ecuador convergent margin and the Carnegie Ridge, possible consequence on great earthquakes recurrence interval, *Geophys. Res. Lett.*, *31*, L04603, doi:10.1029/2003GL018803.

Gutscher, M. A., J. Malavieille, S. Lallemand, and J. Y. Collot (1999), Tectonic segmentation of the North Andean margin: Impact of the Carnegie Ridge collision, *Earth Planet. Sci. Lett.*, *168*, 255–270.

Hirose, H., K. Hirahara, F. Kimata, N. Fujii, and S. Miyazaki (1999), A slow thrust slip event following the two 1996 Hyuganada earthquakes beneath the Bungo Channel, southwest Japan, *Geophys. Res. Lett.*, *26*, 3237–3240.

Holtkamp, S. G., and M. R. Brudzinski (2011), Earthquake swarms in circum-Pacific subduction zones, *Earth Planet. Sci. Lett.*, *305*, 215–225, doi:10.1016/j.epsl.2011.03.004.

Holtkamp, S. G., M. E. Pritchard, and R. B. Lohman (2011), Earthquake swarms in South America, *Geophys. J. Int.*, *187*, 128–146.

Ide, S., G. C. Beroza, D. R. Shelly, and T. Uchide (2007), A scaling law for slow earthquakes, *Nature*, *447*, 76–79.

Kanamori, H., and K. C. McNally (1982), Variable rupture mode of the subduction zone along the Ecuador-Colombia coast, *Bull. Seismol. Soc. Am.*, *72*, 1241–1253.

Kanda, R. V. S., and M. Simons (2010), An elastic plate model for interseismic deformation in subduction zones, *J. Geophys. Res.*, *115*, B03405, doi:10.1029/2009JB006611.

Kato, A., K. Obara, T. Igarashi, H. Tsuruoka, S. Nakagawa, and N. Hirata (2012), Propagation of slow slip leading up to the 2011 M_w 9.0 Tohoku-Oki earthquake, *Science*, *33*, 705–708.

Kelleher, J. (1972), Rupture zones of large South American earthquakes and some predictions, *J. Geophys. Res.*, *77*, 2087–2097.

Kim, M. J., S. Y. Schwartz, and S. Bannister (2011), Non-volcanic tremor associated with the March 2010 Gisborne slow slip event at the Hikurangi subduction margin, New Zealand, *Geophys. Res. Lett.*, *38*, L14301, doi:10.1029/2011GL048400.

Lengliné, O., J. E. Elkhoury, G. Daniel, J. Schmittbuhl, R. Toussaint, J.-P. Ampuero, and M. Bouchon (2012), Interplay of seismic and aseismic deformations during earthquake swarms: An experimental approach, *Earth Planet. Sci. Lett.*, *331–332*, 215–223.

Liu, Y., J. R. Rice, and K. M. Larson (2007), Seismicity variations associated with aseismic transients in Guerrero, Mexico, 1995–2006, *Earth Planet. Sci. Lett.*, *262*, 493–504.

Manchuel, K., M. Régnier, N. Béthoux, Y. Font, V. Sallares, J. Diaz, and H. Yepes (2011). New insights on the interseismic active deformation along the North Ecuadorian-South Colombian (NESC) margin, *Tectonics*, *30*, TC4003, doi:10.1029/2010TC002757.

Mazzotti, S., and J. Adams (2004), Variability of near-term probability for the next great earthquake on the Cascadia subduction zone, *Bull. Seismol. Soc. Am.*, *94*, 1954–1959.

McCaffrey, R., L. M. Wallace, and J. Beavan (2008), Slow slip and frictional transition at low temperature at the Hikurangi subduction zone, *Nat. Geosci.*, *1*, 316–320.

Mendoza, C., and J. Dewey (1984), Seismicity associated with the great Colombia-Ecuador earthquakes of 1942, 1958 and 1979: Implications for barrier models of earthquake rupture, *Bull. Seismol. Soc. Am.*, *74*, 577–593.

Métois, M., A. Socquet, and C. Vigny (2012), Interseismic coupling, segmentation and mechanical behavior of the central Chile subduction zone, *J. Geophys. Res.*, *117*, B03406, doi:10.1029/2011JB008736.

Moreno, M., M. Rosenau, and O. Oncken (2010), 2010 Maule earthquake slip correlates with pre-seismic locking of Andean subduction zone, *Nature*, *467*, 198–202, doi:10.1038/nature09349.

Outerbridge, K. C., T. H. Dixon, S. Y. Schwartz, J. I. Walter, M. Protti, V. Gonzalez, J. Biggs, M. Thorwart, and W. Rabbel (2010), A tremor and slip event on the Cocos-Caribbean subduction zone as measured by a global positioning system (GPS) and seismic network on the Nicoya Peninsula, Costa Rica, *J. Geophys. Res.*, *115*, B10408, doi:10.1029/2009JB006845.

Ozawa, S., S. Miyazaki, Y. Hatanaka, T. Imakiire, M. Kaidzu, and M. Murakami (2003), Characteristic silent earthquakes in the eastern part of the Boso Peninsula, central Japan, *Geophys. Res. Lett.*, *30*(6), 1283, doi:10.1029/2002GL016665.

Payero, J., V. Kostoglodov, N. Shapiro, T. Mikumo, A. Iglesias, X. Pérez-Campos, and R. Clayton (2008), Nonvolcanic tremor observed in the Mexican subduction zone, *Geophys. Res. Lett.*, *35*, L07305, doi:10.1029/2007GL032877.

Peng, Z., and J. Gomberg (2010), An integrated perspective of the continuum between earthquakes and slow-slip phenomena, *Nat. Geosci.*, *3*, 599–607.

Pennington, W. D. (1981), Subduction of the eastern Panama Basin and seismotectonics of northwestern South America, *J. Geophys. Res.*, *86*, 10,753–10,770.

Radiguet, M., F. Cotton, M. Vergnolle, M. Campillo, B. Valette, V. Kostoglodov, and N. Cotte (2011), Spatial and temporal evolution of a long term slow slip event: The 2006 Guerrero slow slip event, *Geophys. J. Int.*, *184*, 816–828.

Rani, S., and S. J. Singh (1992), Static deformation of a uniform half-space due to a long dip-slip fault, *Geophys. J. Int.*, *109*, 469–476.

Rogers, G., and H. Dragert (2003), Episodic tremor and slip on the Cascadia subduction zone: The chatter of silent slip, *Science*, *300*, 1942–1943.

Ruegg, J. C., A. Rudloff, C. Vigny, R. Madariaga, J. B. de Chabalier, J. Campos, E. Kausel, S. Barrientos, and D. Dimitrov (2009), Interseismic strain accumulation measured by GPS in the seismic gap between Constitucion and Concepcion in Chile, *Phys. Earth Planet. Inter.*, *175*, 78–85, doi:10.1016/j.pepi.2008.02.015.

Sagiya, T. (2004), Interplate coupling in the Kanto district, central Japan, and the Boso Peninsula silent earthquake in May 1996, *Pure Appl. Geophys.*, *161*, 2601–2616.

Sato, R. (1972), Stress drop for a finite fault, *J. Phys. Earth*, *20*, 397–407.

Savage, J. C. (1983), A dislocation model of strain accumulation and release at a subduction zone, *J. Geophys. Res.*, *88*, 4984–4996.

Schwartz, S. Y., and J. M. Rokosky (2007), Slow slip events and seismic tremor at circum-Pacific subduction zones, *Rev. Geophys.*, *45*, RG3004, doi:10.1029/2006RG000208.

Segovia, M. (2001), El sismo de Bahia del 4 de agosto de 1998: Caracterizacion del mecanismo de ruptura y analisis de la sismicidad en la zona costera [in Spanish], *tesis de previa a la obtencion del titulo de Ingeniera Geologa*, 126 pp., Esc. Politec. Nac., Quito, Ecuador.

Segovia, M. (2009), Análisis espacio-temporal del Enjambre de Puerto López entre enero y febrero de 2005 con observaciones de la estación de banda ancha de OTAVALO [in Spanish], *Master thesis, Univ. Nice Sophia Antipolis*, Quito, Ecuador.

Singh, S. K. (1977), Slip and stress drop on a circular fault, *Bull. Seismol. Soc. Am.*, *67*, 279–284.

Swenson, J. L., and S. L. Beck (1996), Historical 1942 Ecuador and 1942 Peru subduction earthquakes, and earthquake cycle along Colombia-Ecuador and Peru subduction segments, *Pure Appl. Geophys.*, *146*, 67–101.

Tarantola, A. (2005), *Inverse Problem Theory and Methods for Model Parameter Estimation*, Soc. for Ind. and Appl. Math., SIAM, Philadelphia, Pa.

Theunissen, T., Y. Font, S. Lallemand, and S. Gautier (2012), Improvements of the maximum intersection method for 3D absolute earthquake location, *Bull. Seismol. Soc. Am.*, *102*, 1764–1785.

Tomar, S., and N. K. Dhiman (2003), 2-D deformation analysis of a half-space due to a long dip-slip fault at finite depth, *J. Earth Syst. Sci.*, *112*, 587–596.

Trenkamp, R., J. N. Kellogg, J. T. Freymueller, and P. Mora (2002), Wide plate margin deformation, southern Central America and northwestern South America, CASA GPS observations, *J. South Am. Earth Sci.*, *15*, 157–171.

Vaca, S., M. Regnier, N. Béthoux, V. Alvarez, and B. Pontoise (2009), Sismicidad de la región de Manta (Ecuador): Enjambre sísmico de Manta-2005 [in Spanish with English abstract], in *Geología y geofísica marina y terrestre del Ecuador: desde la costa continental hasta las Islas Galapagos*, pp. 151–166, edited by J.-Y. Collot, V. Sallares, and N. Pazmino, CNDM, IRD, INOCAR, Guayaquil (ECU), Marseille (FRA).

Vidale, J. E., A. J. Hotovec, A. Ghosh, K. C. Creager, and J. Gomberg (2011), Tiny intraplate earthquakes triggered by nearby episodic tremor and slip in Cascadia, *Geochem. Geophys. Geosyst.*, *12*, Q06005, doi:10.1029/2011GC003559.

Wallace, L. M., and J. Beavan (2010), Diverse slow slip behavior at the Hikurangi subduction margin, New Zealand, *J. Geophys. Res.*, *115*, B12402, doi:10.1029/2010JB007717.

Wdowinski, S., Y. Bock, J. Zhang, P. Fang, and J. Genrich (1997), Southern California permanent GPS geodetic array: Spatial filtering of daily positions for estimating coseismic and postseismic displacements induced by the 1992 Landers earthquake, *J. Geophys. Res.*, *102*, 18,057–18,070.

White, S. M., R. Trenkamp, and J. Kellogg (2003), Recent crustal deformation and the earthquake cycle along the Ecuador-Colombia subduction zone, *Earth Planet. Sci. Lett.*, *216*, 231–242.